ORIGINAL ARTICLE

Impact of the intense geomagnetic storm of August 2018 on the equatorial and low latitude ionosphere

Nadia Imtiaz[1] · Omar Hammou Ali[2] · Haider Rizvi[1]

Abstract

We study the impact of an intense geomagnetic storm of 25–26 August 2018 on the equatorial and low latitude ionosphere over Asia, Africa, and America. For this purpose, we have used storm-time observations from multi-site ground-based Global Positioning System receivers and magnetic observatories located at equatorial and low latitudes along the three longitudes. The storm-time variation of the electron density is assessed by the global, regional, and vertical total electron content obtained from the GPS receiver data. Both positive phases of the storm and negative ones are observed in the three longitudinal sectors during the main phase until the late recovery phases of the storm. A significant increase in the electron density around the equatorial ionization anomaly crests is seen during the main phase of the storm. The storm-time response of the thermosphere is characterized by the global $\frac{O}{N_2}$ maps provided by the Global Ultraviolet Spectrographic Imager onboard the satellite Thermosphere Ionosphere Mesosphere Energetics and Dynamics. The expected hemispheric asymmetry of the thermosphere can be associated with possible differences in heating and convection in the middle and lower latitudes. Moreover, the unprecedented behavior of the neutrals over the East-African and Asian longitudes can be attributed to the strong northward meridional wind circulations. Finally, the storm-induced disturbances of the horizontal component of the Earth's magnetic field and the ionospheric electric currents have been investigated by ground-based magnetometers data. A large decrease in the horizontal component of the geomagnetic field is observed over the local dayside sector (Asian) that is associated with the enhanced ring current effect. The wavelet analysis of the magnetic data indicates the existence of short-term and diurnal oscillations during the storm period. These oscillations are associated with the prompt penetration and the disturbance of dynamo-electric fields. It can be inferred that physical factors such as the ionospheric electrodynamics, the thermosphere neutral composition, and the neutral wind circulations play an important role in the observed storm-time response of the ionosphere.

Keywords Global electron content · Vertical total electron content · Prompt penetration electric field · Disturbance dynamo electric field

1 Introduction

The Sun-Earth interaction mainly controls the Earth's upper atmosphere that can be perturbed by the space weather events, such as geomagnetic storms. A geomagnetic storm is a temporary disturbance of the geomagnetic field caused by an efficient exchange of energy from the solar wind into the Earth's magnetosphere. The deposition of this energy at high latitudes results into significant disturbances in the

quiet time ionosphere. The coronal mass ejections (CMEs) with specific magnetic field structures emitted by the Sun compress the magnetosphere by exerting a sudden dynamic pressure on the Earth's magnetosphere. As a result, a sharp positive or negative impulse can be observed in the ground currents as recorded by the magnetometers that is referred as sudden storm commencement (SSC) by Curto et al. (2007).

During geomagnetic storms under the southward excursion of the B_z component of the interplanetary magnetic field (IMF), the interplay between the solar wind and Earth's magnetosphere can modify the poleward field aligned current (FAC). It leads to a sudden increase in the dawn-to-dusk polar cap potential. The equatorward FAC in the inner magnetosphere cannot shield the mid-latitude and equatorial lat-

---

✉ N. Imtiaz

[1] Theoretical Physics Division, PINSTECH Islamabad, Pakistan

[2] Geophysical Laboratory, FSTGAT, B.P.32 USTHB, 16123 Bab-Ezzouar, Algeria

itudes from the high-latitude electric fields. As a result, the electric field from the high latitude instantaneously penetrates into the middle and the equatorial ionosphere. This is known as the prompt penetration electric field (PPEF) Kikuchi et al. (1978), Kelley et al. (1979). The reported effect of the PPEF at the equatorial ionosphere during substorms is short, ca. 30 min, which is equivalent to the magnetospheric shielding time constant Nishida (1968), Spiro et al. (1988), Fejer (1991). However, the effect of the PPEF can exist for a longer time during an extended period of a strong geomagnetic activity. An evidence of a long duration penetration of the interplanetary electric field (IEF) to the low-latitude ionosphere without shielding is provided by Huang et al. (2005). The high-latitude ionosphere electrodynamics is strongly affected by this IEF, which further leads to various electric fields, and also by the polar plasma convection Gonzalez et al. (1994). It induced ionospheric electric fields, including the equatorial PPEF, the disturbance dynamo electric field (DDEF), the equatorial polarization, and the sub-auroral polarization stream (SAPS) Nishida (1968), Blanc and Richmond (1980), Balan and Bailey (1995). The PPEFs observed in the equatorial latitudes can cause convection of the ionosphere plasma upward in the dayside and downward in the nightside.

During intense geomagnetic storms, the PPEFs are larger than the fields associated with the normal fountain effect. This can cause lifting of the dayside equatorial plasma to higher altitudes and latitudes compared to its normal position, such that the crests of the equatorial ionospheric anomaly (EIA) can reach the middle latitudes. It is called the dayside ionospheric super fountain (DIS) effect Tsurutani et al. (2004, 2008). At high latitudes, the precipitation of the energetic particles into the thermosphere also enhances the ionospheric conductivities that can generate the strong electrical currents Buonsanto (1999). The dissipation of these currents can cause heating and expansion of the auroral zone due to the Joule effect that can modify the lower thermospheric composition and can drive the large-scale neutral winds Fuller-Rowell et al. (1994), Danilov (2001). Therefore, the combination of these different interacting physical processes during major geomagnetic storms can lead to a large-scale thermal plasma redistribution involving the equatorial latitudes through the polar ones.

The storm-time response of the distinct ionospheric regions is different as various physical mechanisms are involved in the modification of the electron density in these regions. For example, the D and E regions exhibit a significant enhancement of electron density in the auroral zone due to increased energetic particles' precipitation Lastovicka (1997). On contrary, the F2 region exhibits a very complicated spatial and temporal behavior during geomagnetic storms Danilov (2001). It shows both positive and negative phases depending on different mechanisms associated with

the ionospheric electrodynamics and the neutral composition variation. The positive phase of ionospheric storm refers to a storm-time increase and the negative one to a decrease in the electron density relative to the quiet-time level.

One of the tools for a better understanding of the spatial and temporal ionospheric variability induced by geomagnetic storms is the Global Navigation Satellite System (GNSS) receivers. For monitoring ionospheric total electron content (TEC) based on ground GNSS receivers the International GNSS Service (IGS), consisting of four IGS Ionospheric Associate Analysis Centers (IACCs), was established in 1998. These are the Center for Orbit Determination in Europe (CODE), the Jet Propulsion Laboratory (JPL), the European Space Agency (ESA), and the Polytechnic University of Catalonia (UPC) Ren et al. (2016). These centers use data from different IGS sites to produce Global ionosphere maps (GIMs) of vertical total electrons content (vTEC) that provide reliable information about the ionosphere Hernandez-Pajares et al. (2009). Several studies used GPS-TEC data to investigate the storm-time response of the ionosphere due to the southward excursion of the IMF. These studies show a significant increment in the equatorial and mid-latitude TEC during geomagnetic storms Huang et al. (2005), Mannucci et al. (2005), Astafyeva (2009). This turns into an enhancement of the TEC in equatorial ionization anomaly (EIA) that can be visualized in the GIMs Appleton (1946), McDonald et al. (2011).

Besides ground-based observations, the space-borne measurements of the neutral composition can also be analyzed to understand the physical processes responsible for the observed storm effects. For this purpose, the Global Ultraviolet Imager (GUVI) onboard the TIMED spacecraft provides global measurements of the far ultraviolet dayglow intensity Paxton et al. (2004). These measurements provide an estimate of the atmospheric $\frac{O}{N_2}$ concentration that affects the ionization in the upper atmosphere. The physical mechanism of atmospheric upwelling is described by Prölls (1995). During storms, the $\frac{O}{N_2}$ ratio tends to decrease at high latitudes Prölls (1995), Meier et al. (2005), Zhang et al. (2004). Moreover, the $\frac{O}{N_2}$ ratio can also alter the thermosphere-ionosphere plasma density at mid and low latitudes during geomagnetic storms. In this context, Ratovsky et al. (2018) reported that the positive TEC disturbance in after-storm phases is associated with an increase in the atomic oxygen due to its transport from equatorial to middle latitudes. Ramsingh et al. (2015) and Ramsingh and Sripathi (2017) analyzed data from ground-based Ionosondes and GPS receivers over India to investigate the equatorial and low latitude ionosphere response to the intense geomagnetic storms of the solar cycle 24.

Recently, the ionospheric response to the 26 August 2018 geomagnetic storm based on the GPS-TEC observations along 80° E and 120° E longitudes in the Asian sector

Table 1 Geographic and geomagnetic locations of the GPS stations located in different regions used in the analysis

Station	Country	GLAT (MLAT)	GLONG (MLONG)
Karratha (KARR)	Asia	20.98° S (38.35° S)	117.10° E (170.85° W)
Putrajaya (ANMG)	Asia	2.79° N (16.03° S)	101.51° E (179.68° E)
Hanoi (JNAV)	Asia	21.01° N (30.23° N)	105.89° E (172.23° W)
Windhoek (WIND)	Africa	22.57° S (22.09° S)	17.09° E (86.00° E)
N'KOLTANG (NKLG)	Africa	0.35° N (1.59° N)	09.67° E (82.67° E)
Dakr (DAKR)	Africa	14.72° N (36.43° N)	17.44° W (94.94° E)
Iquique (IQQE)	America	20.27° S (27.58° S)	70.13° W (1.18° E)
Quito (QUI)	America	0.22° N (6.82° S)	78.45° W (1.30° E)
Observatorio Geodinamico-Centro Nacional (SCUB)	America	20.01° N (14.19° N)	75.76° W (1.27° W)

was presented by Lissa et al. (2020). They observed a large positive storm effect in the daytime TEC during the period starting from the main phase until the late recovery phase of the storm. However, the TEC response between the two longitudes exhibits significant differences, particularly during the recovery phase of the storm that is also confirmed by GIM-derived TEC. The equatorial ionization anomaly (EIA) also shows a strong enhancement around the anomaly crests during the main phase of the storm. In this paper, we analyze the response of the equatorial and low latitude ionosphere over three longitudes, which are American, African, and Asian, to the geomagnetic storm of 26 August 2018. The storm effects are analyzed by the approach applied for the analysis of the geomagnetic storms of March 2015, June 2015, and September 2017 as presented by Nava et al. (2016), Kashcheyev et al. (2018), Imtiaz et al. (2020). We analyzed the response of diverse parameters using the data from the ground-based instruments (Global Positing System receivers and magnetometers) and from the instrument (Global Ultra Violet Spectrographic Imager (GUVI)) onboard the satellite Thermosphere Ionosphere Mesosphere Energetics and Dynamics (TIMED). On the basis of our analysis, we also tried to explain the unprecedented hemispheric asymmetries during ionospheric storm of 24–25 August 2018 as mentioned by Astafyeva et al. (2020). The manuscript is organized in the following manner: Sect. 2 contains the description of data sets used and their analysis techniques; Sect. 3 describes the space weather event under consideration; Sect. 4 presents the results and discussion; and, finally, Sect. 5 summarizes our results.

2 Methodology

To study the impact of the space weather event of 25–26 August 2018 on the equatorial and low latitude ionosphere, we analyzed multi instrument data, including the solar wind parameters, the GPS-TEC, the thermosphere neutral composition, and the magnetometers over the three consecutive longitudes, which are Asian, African, and American. Here, we present these data sets and their analysis techniques.

2.1 Solar wind data

The solar wind parameters such as B_z component of the IMF, the solar wind speed (V_{sw}), the proton number density (n_p), and the electric field (E_y) have been obtained from the OMNI database. The information about the geomagnetic indices is provided by the world data center for Geomagnetism (WDC); (http://wdc.kugi.kyoto-u.ac.jp). It includes the 3-h Kp index, which depicts the disturbance in the horizontal component of the geomagnetic field, and the high-resolution SYM(H) index, which estimates the growth/decay of the storm time ring current Rostoker (1972), Wanliss and Showalter (2006). The north and south polar cap (PCN/PCS) indices represent the energy input into the magnetosphere and give a quantitative estimate of the geomagnetic activity at the polar latitudes Stauning et al. (2008).

2.2 GPS data and global ionosphere maps (GIMs)

The storm-time ionospheric variability can be assessed by the TEC data obtained from the GPS receiver stations located from equatorial (0° : 10° N) to low latitude (10° : 30° N) in the three longitudes given as Asian (60° : 150° E), African (30° W: 60° E), and the American (150 : 30° W). The geographic and geomagnetic locations of the selected stations are given in Table 1. The storm-time vTEC response in the three sectors is analyzed by the 15-min time resolution data extracted from the IGS Global Ionosphere Map (GIM) data available in the IONEX format for the entire globe (ftp://cddis.gsfc.nasa.gov/gps/products/ionex/2018). The spatial resolution of each GIM is 2.5° in latitude and 5° in longitude, respectively. Therefore, each ionosphere map contains 5,184 data points known as GIM cells.

Table 2 Geographic and geomagnetic locations of the Magnetometers used in the analysis

Station	Country	GLAT (MLAT)	GLONG (MLONG)
GUAM (GUA)	Asia	13.59° N (5.87° N)	144.87° E (143.28° W)
TAMANRASSET (TAM)	Africa	22.79° N (22.79° N)	5.53° W (58.16° E)
SAN JUAN (SJG)	America	18.28° N (27.62° N)	66.6° W (6.95° E)

The GIMs are used to compute the global and regional total electron content (GEC/REC). The global electron content (GEC) represents the total number of electrons presented in the near-Earth space environment, and its unit is $1 \text{GECU} = 10^{32}$ electrons. It is a useful parameter that can be used to analyze the global features of the ionosphere during the storm period. The storm time variation of the GEC can be assessed by the tomographic kriging GIMs as provided by the Technical University of Catalonia (UPC). From the 15-min time resolution data of the UPC-GIM, the GEC can be obtained as given by Afraimovich et al. (2008),

$$GEC = \sum_{i,j} I_{i,j} . S_{i,j},$$

where $I_{i,j}$ is a cell containing the vTEC value, the $S_{i,j}$ is corresponding cell area with i and j representing the latitude and longitude of a certain GIM cell, respectively. As mentioned earlier, the latitudinal and longitudinal extent of the elementary GIM cell is 2.5° and 5°, respectively. The regional electron content (REC) represents the number of electrons presented over the specific region, such as Asia, Africa, and America. It is used to analyze the relative contribution of different regions to the GEC. In order to compute the REC variations, the GEC can be subdivided into the three longitudinal sectors. It is computed similarly to the GEC with the summation being restricted to the GIM cells of that particular region.

2.3 GUVI/TIMED data

The O/N_2 ratio represents thermosphere neutral composition, which plays an important role in the production and loss of the ionospheric F-region plasma. Therefore, it can help to understand the storm-time ionospheric variability Rishbeth (1998), Zhang et al. (2004), Lei et al. (2010), Cai et al. (2020). We also analyzed the $\frac{O}{N_2}$ maps obtained from TIMED/GUVI measurements to understand the contribution of the global thermospheric neutral compositions to the ionospheric disturbances induced by the storm of 25–26 August 2018.

2.4 Magnetometers data

The storm-related geomagnetic field variations are analyzed by the quasi-definitive data obtained from the magnetic observatories located in the three selected longitudinal sectors.

The data of these magnetic observatories are available at http://www.intermagnet.org. The geographic and geomagnetic coordinates of these observatories are given in Table 2. The storm-related variation of the horizontal component H of the geomagnetic field can be calculated as proposed by Nava et al. (2016), Kashcheyev et al. (2018):

$$H = H_o + S_R + D_m + Diono,$$

where H_o depicts the magnetic field produced in the Earth's core and crust, S_R represents the quiet daily variation of the geomagnetic field given as $S_q = < S_R >$, D_m is the disturbance related to the magnetospheric currents and Diono is the magnetic field variations associated with the disturbed ionospheric currents.

The S_q can be calculated from the average value of ΔH_i through the following expression:

$$S_{qi} = \frac{1}{n} \sum_{j=1}^{n} \Delta H_i^j,$$

where j represents a day number, n is a total number of quiet days, and ΔH is the variation of the horizontal component (H) of the magnetic field, that is, $\Delta H_i = H_i - H_o$, H_o represents the baseline value with i = 1 to 1440 min. The H_o is an average of the hourly values at midnight (LT) that is given by:

$$H_o = \frac{H_{22}^j + H_{23}^j + H_{00}^{j+1} + H_{01}^{j+1}}{4}.$$

The hourly amplitude of the S_q, including the non-cyclic variation, can be calculated as given by Matsushita and Campbell (1967):

$$\Delta NC = \frac{H_{00}^{j+1} - H_{00}^j}{24}.$$

The corrected hourly solar quiet variation $S_q(H)$ can be expressed as:

$$S_{qi}(H) = S_{qi} + \frac{i \Delta NC}{60},$$

where i = 1 to 1440 min.

The D_m can be estimated by the following expression:

$$D_m = SYM(H) \times \cos \phi,$$

where ϕ is the geomagnetic latitude.

Therefore, the final expression for Diono becomes:

$$Diono = \Delta H - S_q - SYM(H) \times \cos\phi,$$

where ΔH is the variation of the H component of the Earth's magnetic field, the SYM(H) index is the estimation of the symmetric part of the ring current and ϕ represents the geomagnetic dip latitude. Diono account for the combine effects of the disturbance polar no. 1 (DP1), the disturbance polar no. 2 (DP2), the disturbance polar no. 3 (DP3), the disturbance polar no. 4 (DP4), and ionospheric disturbed dynamo currents (Ddyn). At low and middle latitudes, the expression for dayside Diono is given by Kashcheyev et al. (2018), Younas et al. (2020),

$$Diono = DP2 + Ddyn.$$

It can be noticed that the above expression for Diono does not contain contribution from the polar disturbances DP1, DP3 and DP4 because the effect of these disturbances is ignorable on dayside low-to-middle latitude ionosphere Amaechi et al. (2020). The storm-time variations in the H component and Diono are computed from the data of individual station.

3 Space weather event description

We consider the space weather event that caused a strong geomagnetic storm of G3 class (Kp = 7) on 26 August 2018. A brief description of this space weather event is given below.

On 20 August 2018, a slow CME with earthward trajectory is emitted by the filament eruption that was observed on the same day at 8:00 UT. Upon reaching the Earth, this CME causes the onset of sudden storm commencement (SSC) around 9:00 UT on 25 August 2018. The storm time variations in the interplanetary and geomagnetic parameters corresponding to this geomagnetic disturbance are shown in Fig. 1 in the following order from top to bottom: the Bz component of the IMF, the Ey component of the interplanetary electric field (IEF), the SYM(H) index, the solar wind speed (V_{sw}), the proton number density (n_p), the Kp index, and the north/south polar cap indices (PCN/PCS). The red vertical line represents the CME reaching the Earth, which lead to the SSC at 9:00 UT on 25 August 2018 as reported by NOAA.

The main phase of the storm starts with the southward turning of the IMF around 15:00 UT on 25 August 2018 and lasts for 14 h. During the main phase, the Bz component of the IMF turns southward and reaches a strongly negative value of about -18.10 nT at 13:09 UT, and it remains southward till the recovery of the storm phase starts on 26 August 2018. The recovery phase of this storm starts with the northward turning of the Bz component of the IMF on 26 August 2018 at 7:11 UT. During the storm recovery phase, the

Bz component of the IMF shows northward and southward oscillations with the three positive peaks in the intervals of 10:00–13:00 UT, 14:00–17:00 UT, and 19:00–20:00 UT. Afterward, the Bz component decreases gradually, and it remains around 0 nT from late 26 August till 31 August 2018. Figure 1b illustrates the storm-time variations in the Ey component of the IEF, which is given as $\tilde{E} = -\tilde{V}_{sw} \times \tilde{B}$. Clearly, it depends on the Bz component of the IMF and on the x component of the V_{sw}. During the main phase of the storm, the southward IMF leads to the eastward IEF with the peak value of $+7.56$ mV/m at 05:06 UT on 26 August 2018. During the recovery phase of the storm, the northward IMF leads to the westward IEF and the IEF-Ey attains the strong negative value of about -7 mV/m on 13:09 UT 26 August 2018. The IEF-Ey shows rapid fluctuation between -5 mV/m and $+6$ mV/m with the positive and negative excursion of the Bz component of the IMF till the end of 26 August 2018. Afterward, the IEF-Ey comes back to its quiet-time value. Figure 1c illustrates the storm-time behavior of the SYM(H) index. During the main phase of the storm, the energization of the equatorial ring current leads to the diminution of the geomagnetic field. This decrease in the geomagnetic field is indicated by a drop of the SYM(H) to a strong negative value of -206 nT around 07:11 UT on 26 August 2018. During the recovery phase, the decay of the equatorial ring current leads to the enhancement of the SYM(H) index. However, the slow decay of the ring current causes the slow recovery of the SYM(H) index to the pre-storm value that takes several days. It can be seen that the value of V_{sw} remains 400 km/s during the main phase of the storm as illustrated in Fig. 1d. However, it increases during the storm recovery phase and attains a maximum value of 634 km/s at 17:34 UT on 27 August 2018. Afterward, it shows the decreasing trend and attains its pre-storm value of about 350 km/s on 31 August 2018. The proton number density shows its peak value of 34 m^{-3} at 8:17 UT on 26 August 2018. The Kp index attains a maximum value of about 7.3 at the time when SYM(H) index attains the minimum value on 26 August 2018. The maximum value of the Kp index categorized this geomagnetic disturbance as G3-class. The PC index also shows a strong increase during the southward excursion of the Bz component of the IMF that is the main phase of the storm. The large value of the PC index indicates the energy input from the solar wind into the magnetosphere during re-connection. It can be noticed that besides the main episode of energy input during the main phase of the storm, the PC index shows another episode of the energy input on late 27 August 2018. During the northward excursion of the Bz component, when there is no magnetic re-connection, the transfer of the solar wind energy into the magnetosphere is prohibited. As a result, the value of the PC index decreases and reaches its pre-storm value after 28 August 2018 as shown in Fig. 1f.
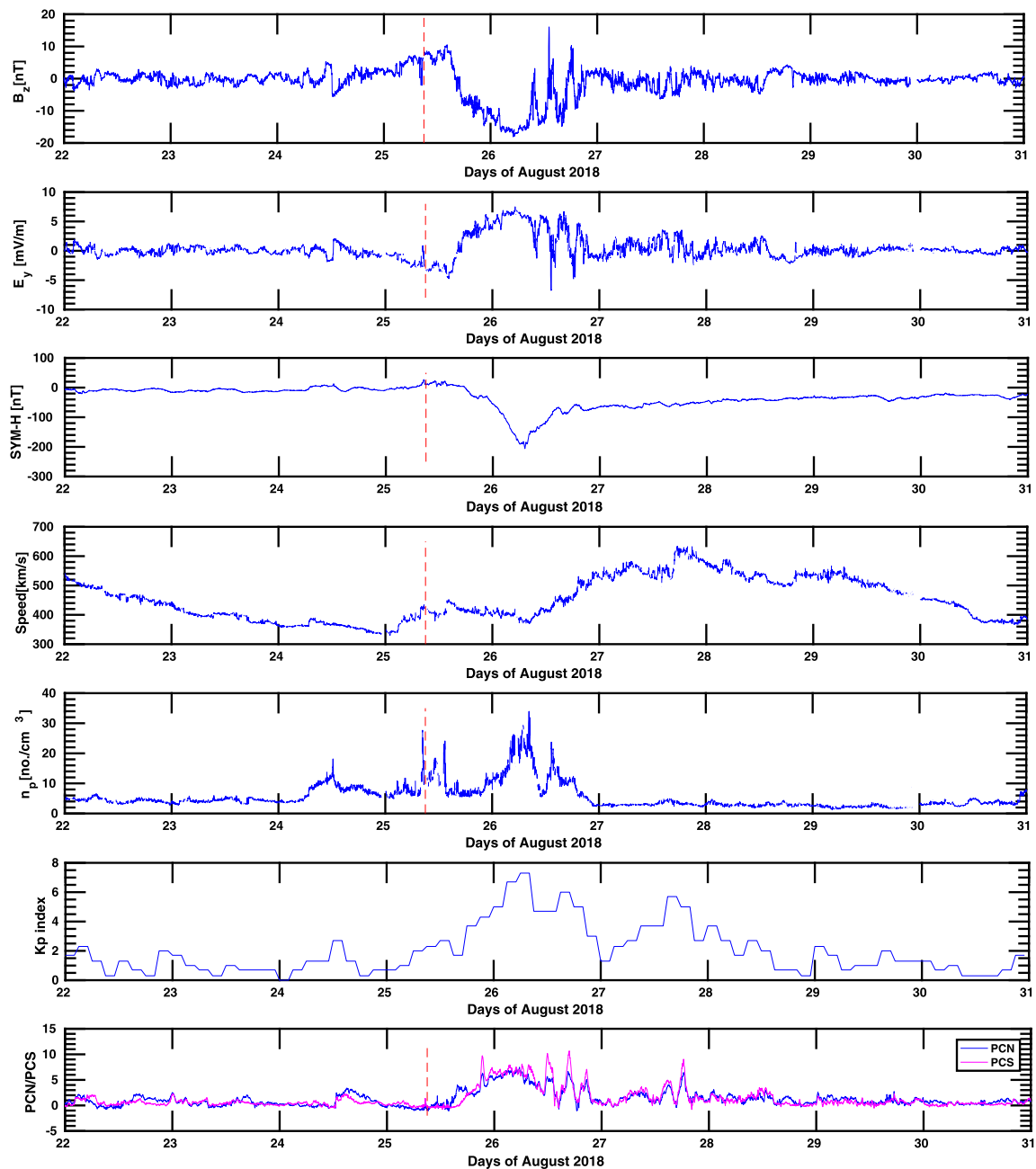
Fig. 1 Solar wind and geomagnetic parameters characterizing the geomagnetic storm during 22–30 August 2018. From a to d: the B_z component of the interplanetary magnetic field, the E_y component of the interplanetary electric field, the SYM(H) index, the solar wind velocity V_{sw} in km/s, the proton number density n_p in cm^{-3}, the K_p index and the polar cap indices PCN/PCS, respectively

4 Results and discussion

In this section, we analyze the impact of the intense geomagnetic storm of 25–26 August 2018 on the equatorial and low latitude Earth's ionosphere by diverse parameters, such as the global ionospheric maps of vertical total electron content, data from the individual Global Navigation Satellite System receivers, the data from ground-based magnetometers, and the thermospheric neutral density maps from the Global Ultraviolet Imager onboard GUVI/TIMED space mission.

Figure 2 shows the variation of the ΔGEC (top) and the ΔREC (bottom) during the period of 22–31 August 2018. Both parameters are computed by subtracting the quiet-time (Kp < 3) variation from the value itself. It can be seen that the ΔGEC have two pronounced peaks of values of

Fig. 2 Variation of the Global electron content (top) and the Regional electron content (bottom) during the period of 22–31 August 2018
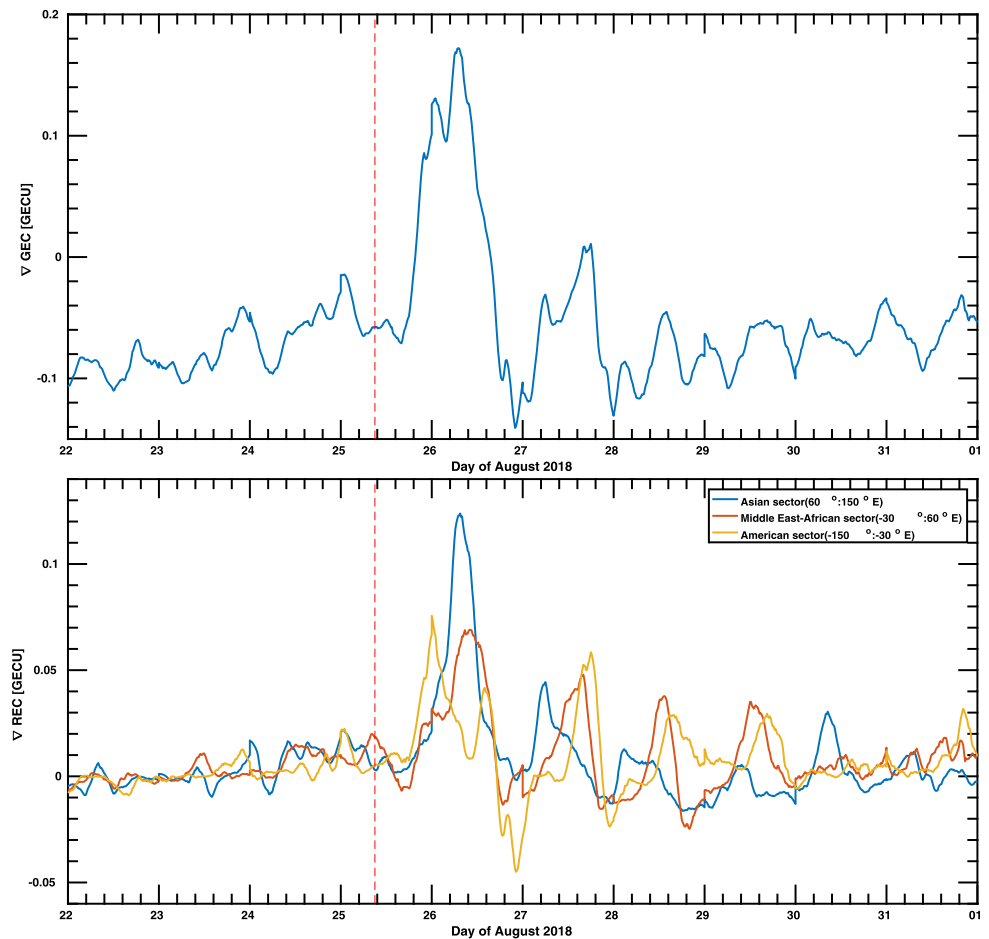

0.12 GECU and 0.16 GECU on 26 August 2018 at 0:00 UT and 07:00 UT, respectively. In order to elucidate the occurrence of these two peaks in the ΔGEC, we plot the ΔREC for the three consecutive longitudinal sectors, Asian, African, and the American. The ΔREC shows significant storm-time enhancement for each longitude that can be identified by the corresponding peak. However, the noticeable feature of the ΔREC for each longitude is the difference in the magnitude and occurrence time of the respective peak during the storm period. Within the main phase of the storm, the response to the large energy input is a strong positive storm effect in the three longitudinal sectors, followed by a small negative storm effect only in the American sector. On the day after the storm, small positive storm effects observed in the three longitudes can be attributed to the small energy input as indicated by the PC index in Fig. 1f. Therefore, it can be inferred that the first peak that appears in ΔGEC during the main phase is due to the positive storm effect in the American sector. The second larger peak is mainly due to the strong positive storm effect in the Asian sector, with a partial contribution that comes from the small positive storm effect in the African sector.

Figure 3 illustrates the storm-time variation of the temporal-latitudinal vTEC maps for Asia (first plot), Africa (second plot), and America (third plot). These vTEC maps are obtained from the IGS GIM data that are available in the IONEX format for the entire globe. For each longitudinal sector, a vTEC map covering the latitudinal range from $-90°$ to $+90°$ can be plotted independently. The corresponding longitudes considered to be $110°$ E for Asia, $-10°$ E for Africa and $-100°$ E for the Americas. The temporal-latitudinal vTEC maps for each sector shown in Fig. 3 cover the period of 22–31 August 2018. These vTEC maps exhibit the following features:

- The Asian sector is in the local midnight side (LT=UT+ 7=2200) at the beginning of the main phase and comes to the local dayside (LT=1400) at the end of the main stage. The vTEC profile exhibits a regular pattern consisting of well-defined northern and southern crests with a clear latitudinal separation of the crests of the anomaly except on the day of the storm. At the beginning of 26 August 2018, a very large storm-time increase in the vTEC can be seen both in the crests and in the trough of the EIA. Also, the latitudinal extent of the EIA increased to about 40°N latitude. This expansion in the EIA can cause

Fig. 3 The vTEC variations over Asia, Africa, and America during the period of 22–31 August 2018
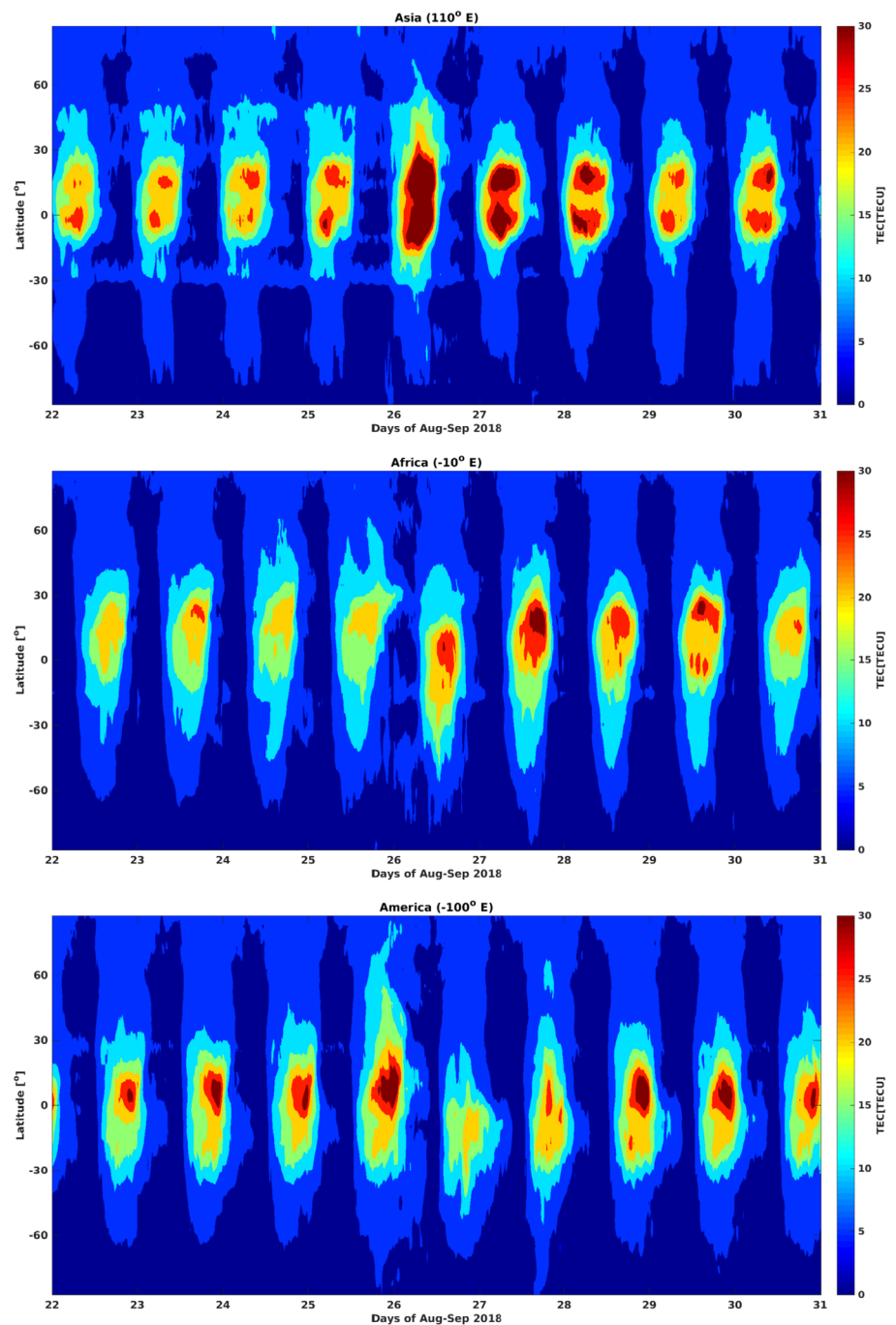
the hemispheric asymmetric storm-time response that was also observed by Astafyeva et al. (2020). During the recovery phase on 27 August 2018, the ionization (vTEC) drops in the equatorial zone. However, a strong enhancement can be observed in the northern/southern crests of the EIA. Moreover, the latitudinal extent of the EIA also drops on this day. After 28 August 2018, the ionization return to the normal pattern as it was before the storm. The observed positive storm effects in the daytime TEC during the main phase over the Asian sector are consistent

with the analysis of GPS-TEC in the equatorial and low latitudes over 80° and 120° longitudes presented by Lissa et al. (2020).

• The African sector is the local dayside sector (LT=UT-1=1400) at the beginning of the main phase and comes to the morning side at the end of the main phase. In this region, the vTEC pattern consists of one crest, which exhibits the varying levels of ionization during the period under consideration. On the day of the storm, an enhancement in the vTEC can be clearly seen in the equatorial

zone. Therefore, most of the vTEC is confined to the equatorial zone in the African sector on 26 August 2018. On the day after the storm, a significant increase in the ionization level of the northern low latitudes can be observed. However, the ionization decreases on the south side of the magnetic equator. Therefore, most of the vTEC is confined to the northern low-latitudes in the African sector on 27 August 2018. After that, the ionization level starts decreasing and returns to its pre-storm value after 28 August 2018.

• The American sector is the local morning sector (LT=UT-5=1000), the vTEC pattern also consists of one crest of ionization with varying levels of ionization during the period under consideration. In contrast to the other two sectors, the vTEC map of the American sector shows a large increase in the vTEC on 25 August 2018 during the main phase of the storm. The ionization level increases in the equatorial zone up to the northern mid-latitudes. On contrary, the southern latitudes show a small increase in the vTEC. During the recovery phase on late 26 August 2018, a strong decrease in the ionization level (vTEC) can be seen over the equatorial and in the northern low latitudes. However, a relatively small increase in the ionization level can be seen over the equatorial and low latitudes on 27 August 2018. Afterward, the vTEC returns to its prestorm pattern. Our analysis of American sector is consistent with the observation in the American and East Pacific sectors reported by Astafyeva et al. (2020).

Figure 4 illustrates the temporal variation in the vTEC for the individual station of the three longitudinal sectors, Asian, African, and American. In Fig. 4, the first three plots represent the stations of the Asian sector (KARR, ANMG, and JNAV), the middle three plots represent the African sector (WIND, NKLG, and DAKR), and the last three plots represent the stations of the American sector (IQQE, QUI, and SCUB). Each plot contains the storm-time variation of the vTEC in the pink curve and the quiet-time daily variation computed by averaging the quiet-time data of the five days prior to the storm (Kp < 3) in the blue curve. During the storm period, the increase or decrease in the vTEC compared with its quiet-time value, also called positive or negative storm effects, can be observed over different stations. The vTEC plot of each station exhibits the following features:

• During the main phase, the positive storm effects with more than 10% increase in the day time vTEC values can be seen over all three stations in the Asian sector. It can be noticed that the equatorial and the northern low latitude stations (ANMG and JNAV) exhibit strong positive storm effect (about +33% and +57% increase in the vTEC) on 26 August 2018. Moreover, both ANMG and JNAV stations show vTEC enhancement till 28 August

2018. However, the southern low latitude station KARR shows a relatively less positive vTEC increase on the day of the storm.

• The three stations in the African sector show less variation in the vTEC during the storm period. For example, the southern low latitude station (WIND) shows a small positive storm effect (+30% increase in vTEC value) during the main phase of the storm. The equatorial station (NKLG) exhibits decrease of about −45% in the vTEC at the beginning of the storm on late 25 August 2018. After that, a small increase of about +20% in the vTEC can be seen for this station on the other days. The northern low latitude station (DAKR) shows a strong decrease of about −60% in the vTEC during the main phase of the storm on 26 August 2018. After that, an enhancement in the vTEC can be observed till 29 August 2018.

• In the American sector, the vTEC over the northern low latitude station SCUB shows an increase of about +60% in the vTEC value at the beginning of the main phase of the storm period. However, the other two stations show a negligible variation in the vTEC at this time. On late 26 August 2018, the negative storm effects in the vTEC can be observed in the equatorial (QUI) (about −35% decrease in the vTEC value) and the northern low latitude stations (SCUB) (about −50% decrease in the vTEC value). Afterward, all three stations show a small increase in the vTEC level till the end of the recovery phase.

• The storm-time response of the three sectors indicates that the local dayside sector, American, responded earlier than the local nightside sector, Asian. Also, the largest increase in the vTEC can be observed in Asia, which is on the nightside at the beginning of the storm. Moreover, the strong negative storm effects can be only seen in the summer hemisphere (Northern Hemisphere here) and the positive storm effects in the winter hemisphere or Southern Hemisphere. These observations of the local time and seasonal dependence of the vTEC agree with the results by Fuller-Rowell et al. (1994) and also with the study on comparison with the two major geomagnetic storms that are: the St. Patrick's day storm of March 2015 and of June 2015 reported by Kashcheyev et al. (2018).

• The highest absolute value of the vTEC observed in this study is about 40 TECU, which is less than that of its value observed during the St. Patrick's day storm that occurred in equinox.

The storm-time changes in the thermospheric neutral gas composition and the neutral wind dynamics can also contribute to the positive and negative ionospheric storm effects at low and equatorial latitudes. The large-scale thermospheric circulation induced by the storm can transport air enriched in atomic oxygen towards the lower latitudes. This enhanced oxygen density affects both ionization production and diffusion that leads to the positive storm effects

Fig. 4 The vTEC variations at equatorial and low latitudes GPS stations during the geomagnetic storm of 22-30 August 2018. Each plot illustrates the disturbed vTEC (in the pink) and its quiet value (in blue)
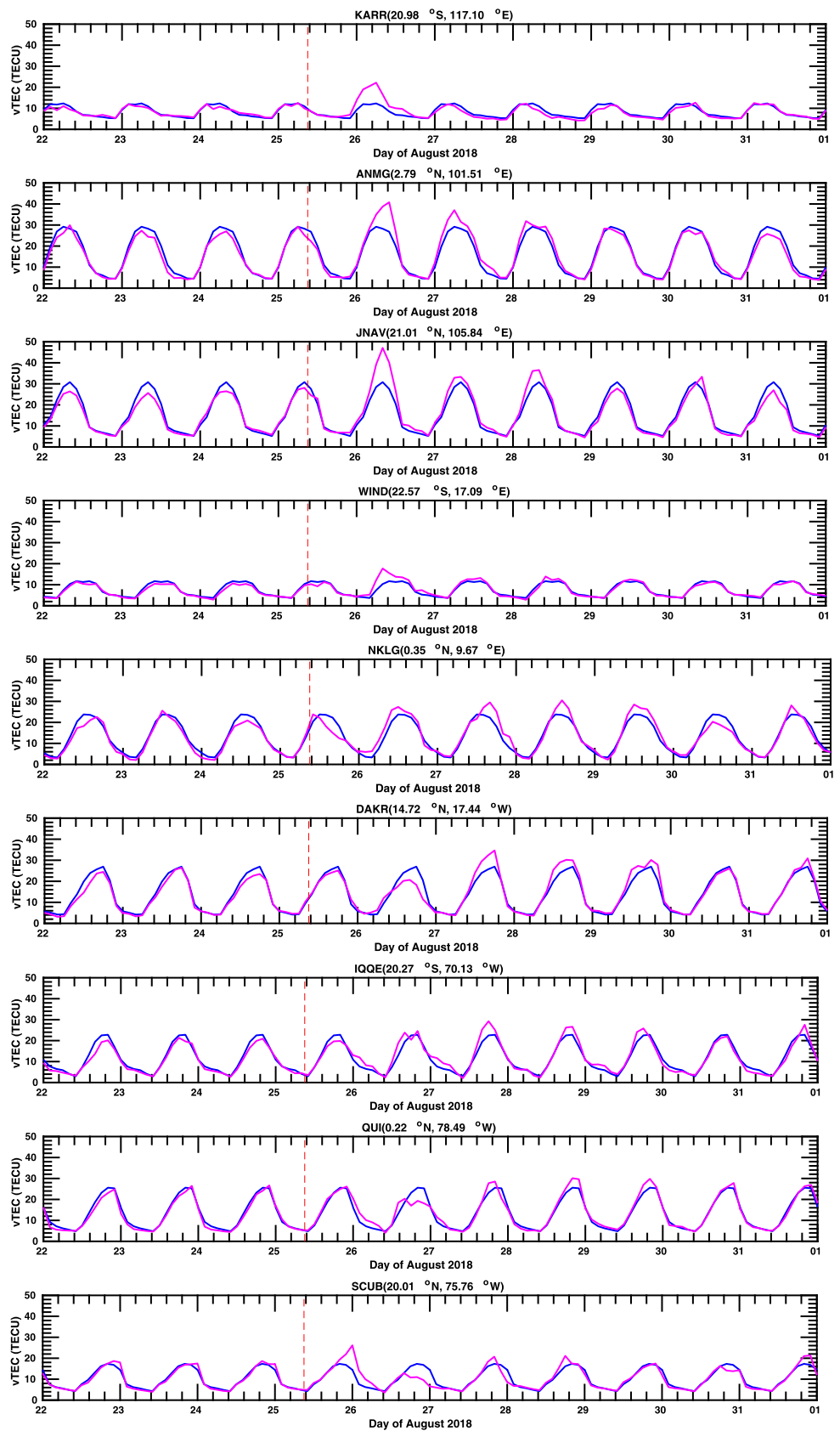
Danilov et al. ([1987](#)), Fuller-Rowell et al. ([1994](#)). Also, a small decrease in the N_2 concentration can also reduce the ionospheric loss rate, which can also increase the electron density. Therefore, an increase in the $\frac{O}{N_2}$ density ratio can increase the electron density and hence, the vTEC Richmond and Lu ([2000](#)), Mansilla ([2006](#)). In order to analyze the storm-time variation of the thermospheric neutral composition, we present the $\frac{O}{N_2}$ density ratio maps of the four consecutive days from 25–28 August 2018 as shown in Fig. [5](#). The following storm-time features of the $\frac{O}{N_2}$ ratio can be observed on 26 August 2018:

- In the Asian sector (60° : 150° E), a strong enhancement in the $\frac{O}{N_2}$ ratio occurs over the equatorial and northern low latitudes. However, a severe depletion in the $\frac{O}{N_2}$ ratio can be seen over the southern low latitudes. The observed behavior of the neutral density composition can be explained by the storm time meridional wind. According to Horizontal Wind Model (HWM), a stronger south-north meridional wind moves neutrals faster to the Northern Hemisphere. This, in turn, leads to an enhanced $\frac{O}{N_2}$ ratio in the northern low latitudes.

- The African sector is divided into two parts that are the West Africa (−30° : 0° E) and the East Africa-Middle East region (0° : 60° E). The thermospheric neutral composition shows storm-time depletion in northern low latitudes and enhancement in southern ones over the West Africa that agrees with Fuller-Rowell et al. ([1996](#)). On contrary, a storm-time increase in the $\frac{O}{N_2}$ ratio can be seen in the northern low latitudes and decrease in southern ones over the East Africa and the Middle East region.

- In the American sector (−150° : −30° E), the $\frac{O}{N_2}$ ratio decreases in the northern low latitudes and increases significantly over the southern low latitudes. The equatorial zone exhibits a relatively small increase in the neutral density on the day of the storm. The storm-time increase in the $\frac{O}{N_2}$ ratio in the southern (winter) hemisphere is consistent with the predictions by Fuller-Rowell et al. ([1996](#)). It is due to a combined effect of the storm-time disturbed atmospheric motion and background solstice circulations, which lead to the confinement of the neutral mass in the Southern Hemisphere or in the winter hemisphere.

- The thermospheric neutral density composition returns to its pre-storm profile after the recovery of the storm.

Figure [6](#) represents the storm-time variations in the geomagnetic field at the low latitude magnetic observatories located in the three longitudinal sectors of Asia (GUA), Africa (TAM), and America (SJG). Each plot shows the three curves corresponding to the variation in the horizontal component of the geomagnetic field (H) (in black), the quiet daily variation (Sq) (in blue) and the ionospheric disturbances (Diono) (in the pink). Initially at the time of SSC, an increase in the H component during the compression of the
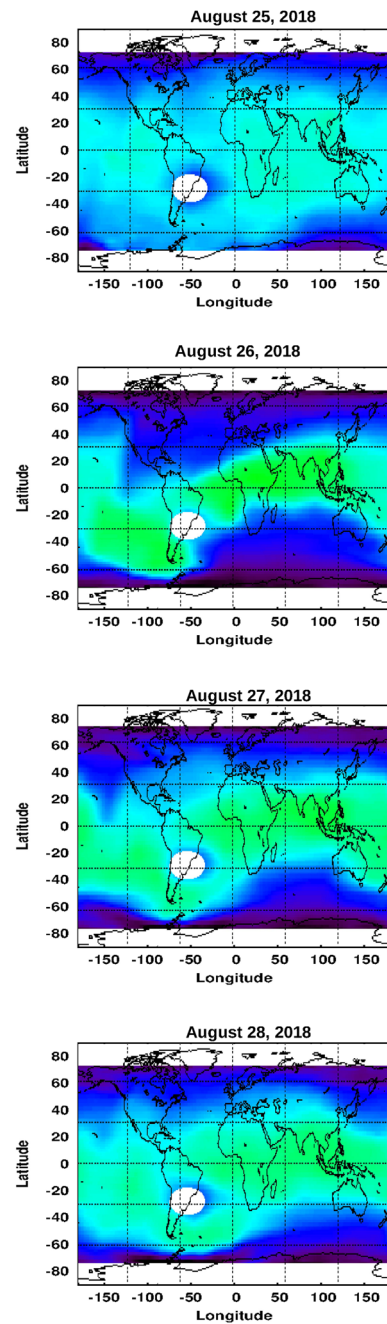
Fig. 5 $\frac{O}{N_2}$ variations over America, Africa, middle East and Asia during four consecutive days on 25–28 August 2018

magnetosphere is related to the Chapman-Ferraro current in Chapman and Ferraro ([1931](#)). During the main phase, a strong decrease in the H component is recorded by the three observatories. This decreasing trend of the H component is related to the diamagnetic behavior of the ring current. The magnetospheric ring current generates the magnetic field opposite to the geomagnetic field. As a result, the H component of the geomagnetic field decreases. During the recovery phase, the ring current decays and the H component returns

Fig. 6 Magnetic field variations over Asia (GUA), Africa (TAM) and America (SJG) during the geomagnetic storm of 25 August 2018
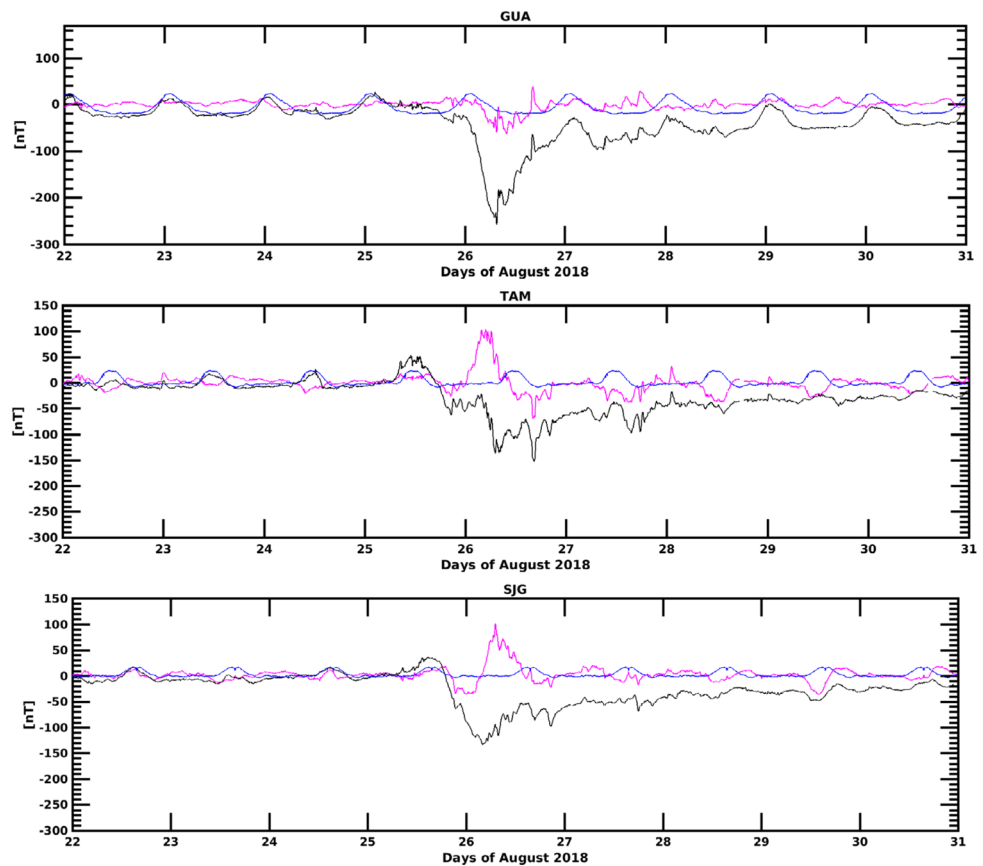
to its pre-storm value. On 26 August 2018, the strongest decrease in the H component of the magnetic field is observed for GUA (-258.82 nT) as compared to the other two stations, e.g., TAM (-152.44 nT) and SJG (-132.78 nT). The following features of the ionospheric electric current disturbance (Diono) can be seen over the three stations:

- During the main phase, the Diono shows the peak values such that 104.38 nT for TAM, 101.54 nT for SJG and 37.44 nT for GUA at different local times. Clearly, the largest value of the Diono is observed for TAM and the smallest for the GUA station.

- Both TAM and SJG show anti-Sq behavior. Also, the Diono oscillations at these two stations persist till 30 August 2018. However, the small oscillations of Diono at GUA decay two days earlier than the other two stations.

Finally, the wavelet transformation has been applied to the Diono and the wavelet power spectrum (WPS) at Asian, African and American sectors as displayed in Fig. 7. Following features can be observed:

- The first and the most prominent feature is the change in the intensity of the power spectrum over the three stations. During the main phase of the storm, an increase in the power of periods between 16–28 h occur over GUA. The African and American stations show enhancement in

the power of periods between 8–28 h and 12–28 h, respectively.

- The second observable feature is the existence of longer oscillations after the day of the storm that is 26 August. For example, the longer oscillations of period of 32 h can last over GUA till 28 August and over SJG and TAM till 29 and 30 August.

- The third feature is the presence of the short oscillations of period of about 2–4 h during the period under consideration. These short period oscillations can be related to the DP2 fluctuations during PPEF and can be obtained by applying high-pass filter as reported by Younas et al. (2020). These perturbations follow the behavior of the Bz oscillations and can penetrate simultaneously at all longitudes. Moreover, the short period oscillations that are not simultaneous can be attributed to the local noise at that station Kikuchi et al. (1996), Khomutov et al. (2017).

5 Summary/conclusion

The impact of an intense geomagnetic storm of 25–26 August 2018 on the equatorial and low-latitude ionosphere over Asian, African and American sectors is presented here. We analyzed diverse parameters including the global, regional, and vertical total electron content derived from the GPS
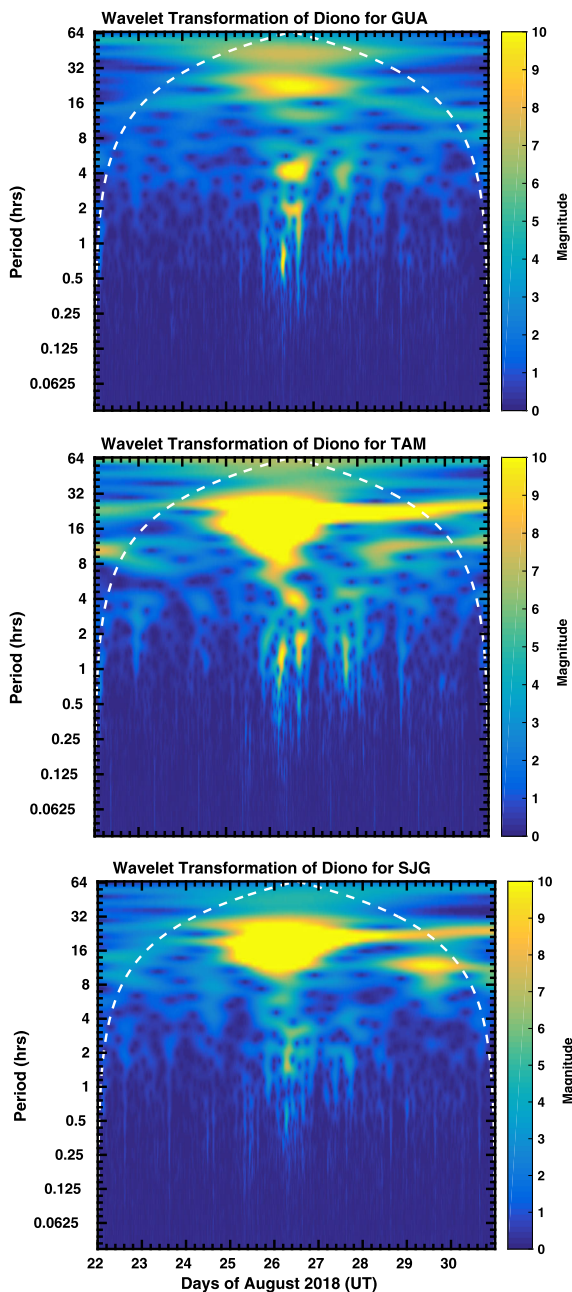
Fig. 7 Wavelet analysis of Diono for Asia(GUA), Africa (TAM), and America (SJG) during the geomagnetic storm of 25 August 2018

data, the geomagnetic field measured at the ground magnetic observatories, and the thermospheric neutral composition obtained from the TIMED/GUVI instrument. Positive and negative storm effects in the vTEC are observed in the local nightside and dayside sectors. The Asian sector exhibits the strongest positive storm time effects in the REC and in the vTEC. However, the American and African sectors show comparatively less storm-time increase in the REC and in the vTEC. Moreover, the temporal response of the three sectors shows that the positive storm effects observed first in the

American sector, followed by the Asian and African sectors. The positive storm effects in the $\frac{O}{N_2}$ are observed in the equatorial zone and northern low latitudes over the East African and Asian sectors. However, the southern low latitudes show negative storm effects. This unprecedented behavior of the $\frac{O}{N_2}$ ratio over East African-Asian longitudes is due to a dominant role of the meridional wind component over these longitudes. The positive storm effects in the $\frac{O}{N_2}$ are observed in the southern low latitudes over West African and American sectors. However, the equatorial zone and the northern low latitudes show negative storm effects over the West longitudes. During the main phase of the storm, the largest disturbance in the amplitude of the horizontal component of the geomagnetic field is observed in Asia (dayside) as compared to that in Africa and America. The wavelet power spectrum of the magnetic field computed for the three sectors indicates the diurnal and short-time oscillations. The diurnal fluctuations last for about four days over the Asian sector and for about six days over the African and American sectors. The short-time oscillations are observed simultaneously over the three sectors on the day of the storm. It can be inferred that these shorter and longer duration oscillations are due to the PPEF and DDEF, respectively.

Declarations

Conflict of Interest The authors declare that they have no conflict of interest.

References

Afraimovich, E.L., Astafyeva, E.I., Oinats, A.V., Yasukevich, Y.V., Zhivetiev, I.V.: Ann. Geophys. **26**, 335–344 (2008)

Amaechi, P.O., Oyeyemi, E.O., Akala, A.O., Amory-Mazaudier, C.: Earth Space Sci. **7**, e2020EA001183 (2020)

Appleton, E.V.: Nature **157**, 691 (1946)

Astafyeva, E.: Ann. Geophys. **27**, 1175–1187 (2009)

Astafyeva, E., Bagiya, M., Forster, M., Nishitani, N.: J. Geophys. Res. **125**(3), e2019JA027261 (2020)

Balan, N., Bailey, G.J.: J. Geophys. Res. **100**, 21421–21432 (1995)

Blanc, M., Richmond, A.D.: J. Geophys. Res. **85**, 1669–1686 (1980)

Buonsanto, M.J.: Space Sci. Rev. **88**, 563–601 (1999)

Cai, X., Burns, A.G., Wang, W., Qian, L., Solomon, S.C., Eastes, R.W., McClintock: Geophys. Res. Lett. **47**(18), e2020GL088838 (2020)

Chapman, S., Ferraro, V.C.A.: Terr. Magn. Atmos. Electr. **36**, 77–97 (1931)

Curto, J.J., Araki, T., Alberca, L.F.: Earth Planets Space **59**, i–xii (2007)

Danilov, A.D.: J. Atmos. Sol.-Terr. Phys. **63**(5), 441–449 (2001)

Danilov, A., Morozova, L.D., Dachev, T.C., Kutiev, I.: Adv. Space Res. **7**(8), 81–88 (1987)

Fejer, B.G.: J. Atmos. Terr. Phys. **53**(N8), 677–693 (1991)

Fuller-Rowell, T.J., Codrescu, M.V., Moffett, R.J., Quegan, S.: J. Geophys. Res. **99**, 3893–3914 (1994)

Fuller-Rowell, T.J., Codrescu, M.V., Rishbeth, H., Moffett, R.J., Quegan, S.: J. Geophys. Res. **101**(A2), 2343–2353 (1996)

Gonzalez, W.D., Joselyn, J.A., Kamide, Y., Kroehl, H.W., Rostoker, G., Tsurutani, B.T., Vasyliunas, V.M.: J. Geophys. Res. **99**(A4), 5771–5792 (1994)

Hernandez-Pajares, M., Juan, J.M., Sanz, J., Orus, R., Garcia-Rigo, A., Feltens, J., Komjathy, A., Schaer, S.C., Krankowski, A.: J. Geod. **83**, 263–275 (2009)

Huang, C.-S., Foster, J.C., Kelley, M.C.: J. Geophys. Res. Space **110**, 13 (2005)

Imtiaz, N., Younas, W., Khan, M.: Ann. Geophys. **38**(2), 359–372 (2020)

Kashcheyev, A., Migoya-Orue, Y., Amory-Mazaudier, C., Fleury, R., Nava, B., Alazo-Cuartas, K., Radicella, S.M.: J. Geophys. Res. **123**, 5000–5018 (2018)

Kelley, M.C., Fejer, B.G., Gonzalez, C.A.: Geophys. Res. Lett. **6**, 301–304 (1979)

Khomutov, S.Y., Mandrikova, O.V., Budilova, E.A., Arora, K., Manjula, L.: Geosci. Instrum. Method. Data Syst. **6**(2), 329–343 (2017)

Kikuchi, T., Araki, T., Maeda, H., Maekawa, K.: Nature **273**, 650–651 (1978)

Kikuchi, T., Lühr, H., Kitamura, T., Saka, O., Schlegel, K.: J. Geophys. Res. **101**(17), 161–173 (1996)

Lastovicka, J.: Stud. Geophys. Geod. **41**, 73–81 (1997)

Lei, J., Thayer, J.P., Burns, A.G., Lu, G., Deng, Y.: J. Geophys. Res. **115**, A05303 (2010)

Lissa, D., Srinivasu, V.K.D., Prasad, D.S.V.V.D., Niranjan, K.: Adv. Space Res. **66**(6), 1427–1440 (2020)

Mannucci, A.J., Tsurutani, B.T., Iijima, B.A., Komjathy, A., Saito, A., Gonzalez, W.D., Guarnieri, F.L., Kozyra, J.U., Skoug, R.: Geophys. Res. Lett. **32**, 4 (2005)

Mansilla, G.A.: J. Atmos. Sol.-Terr. Phys. **68**, 2091–2100 (2006)

Matsushita, S., Campbell, W.H.: pp. 793–819. Academic Press, New York (1967)

McDonald, S.E., Coker, C., Dymond, K.F., Anderson, D.N., Araujo-Pradere, E.A.: Radio Sci. **46**, 1–9 (2011)

Meier, R., Crowley, G., Strickland, D.J., Christensen, A.B., Paxton, L.J., Morrison, D., Hackert, C.L.: J. Geophys. Res. **110**, A09S41 (2005)

Nava, B., Zuluaga, J.R., Alazo-Cuartas, K., Kashcheyev, A., Migoya-Orue, Y., Radicella, S.M., Mazaudier, C.A., Fleury, R.: J. Geophys. Res. **121**, 3421–3438 (2016)

Nishida, A.: Geophys. Res. **73**, 1795–1803 (1968)

Paxton, L.J., et al.: Proc. SPIE Int. Soc. Opt. Eng. **5660**, 227–240 (2004)

Prölls, G.W.: In: Volland, H. (ed.): Handbook of Atmospheric Electrodynamics, vol. 2, pp. 195–248. CRC Press, Boca Raton (1995)

Ramsingh, S., Sripathi, S.: J. Geophys. Res. Space Phys. **122**(11), 645–664 (2017)

Ramsingh, Sripathi, S., Sreekumar, S., Banola, S., Emperumal, K., Tiwari, P., Kumar, B.S.: J. Geophys. Res. Space Phys. **120**(10), 864–910 (2015). 882

Ratovsky, K.G., Klimenko, M.V., Klimenko, V.V., Chirik, N.V., Korenkova, N.A., Kotova, D.S.: Sol.-Terr. Phys. **4**(4), 26–32 (2018)

Ren, X., Zhang, X., Xie, W., et al.: Sci. Rep. **6**, 33499 (2016)

Richmond, A.D., Lu, G.: J. Atmos. Sol.-Terr. Phys. **62**, 1115–1127 (2000)

Rishbeth, H.: J. Atmos. Terr. Phys. **60**(14), 1385–1402 (1998)

Rostoker, G.: J. Geophys. Res. **10**, 935–950 (1972)

Spiro, R.W., Wolf, R.A., Fejer, B.G.: Ann. Geophys. **6**, 39–50 (1988)

Stauning, P., Troshichev, O., Janzhura, A.: J. Atmos. Sol.-Terr. Phys. **70**(18), 2246–2261 (2008)

Tsurutani, B., Mannucci, A., Iijima, B., Abdu, M.A., Sobral, J.H.A., Gonzalez, W., Guarneri, F., Tsuda, T., et al.: J. Geophys. Res. **109**, A08302 (2004)

Tsurutani, B.T., Verkhoglyadova, O.P., Mannucci, A.J., Saito, A., Araki, T., Yumoto, K., Tsuda, T., Abdu, M.A., Sobral, J.H.A., Gonzalez, W.D., McCreadie, H., Lakhina, G.S., Vasyliunas, V.M.: J. Geophys. Res. **113**, A05311 (2008)

Wanliss, J.A., Showalter, K.M.: J. Geophys. Res. **111**, 2005JA011034 (2006)

Younas, W., Amory-Mazaudier, C., Khan, M., Fleury, R.: J. Geophys. Res. **125**(8), 2020JA027981 (2020)

Zhang, Y., Paxton, L.J., Morrison, D., Wolven, B., Kil, H., Meng, C.-I., Mende, S.B., Immel, T.J.: J. Geophys. Res. **109**, A10308 (2004)